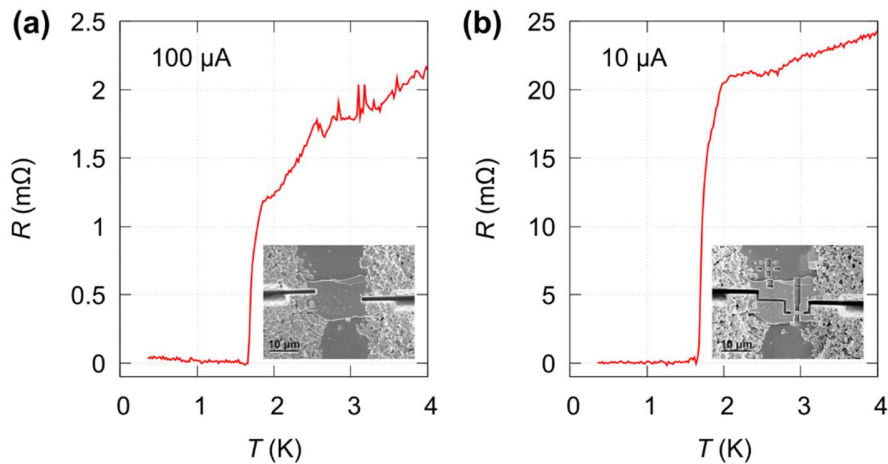


Spontaneous emergence of Josephson junctions in homogeneous rings of single-crystal Sr_2RuO_4

Supplementary Note 1.

EFFECT OF RING STRUCTURING ON RING A

Here, we compare the effect of ring structuring to its superconductivity. Before the ring structuring, we milled the silver paint with focused ion beam (FIB) to make the four-wire configuration (Supplementary Figure 1a inset). Supplementary Figure 1 shows the resistance before/after the ring structuring. The transition temperatures T_c , where the resistance become zero, are not affected by the ring structuring. We note the zero-resistance T_c of (a) is already slightly higher than 1.5 K.



Supplementary Figure 1. Resistance as a function of temperature $R(T)$. (a) $R(T)$ before and (b) after ring structuring (Ring A). The zero-resistance T_c is unchanged by the ring structuring.

Supplementary Note 2.

THEORY

A. Theoretical formalism

The order parameter according to the irreducible representation that breaks the time-reversal symmetry in the crystallographic group of strontium ruthenate (C_{4v}) can be written in the form

$$\Delta(\mathbf{r}, \mathbf{k}) = \eta_+(\mathbf{r})k_+ + \eta_-(\mathbf{r})k_-, \quad (\text{S1})$$

where $k_{\pm} = (k_x \pm ik_y)/k_F$ are chiral basis functions in two dimensions, k_F is the Fermi wave vector, and $\eta_{\pm}(\mathbf{r})$ are the space-dependent components of the order parameter. The differential equations satisfied by the components $\eta_{\pm}(\mathbf{r})$ are obtained from the minimization of the Ginzburg-Landau functional of p -wave superconductivity [1]:

$$\begin{aligned} \mathcal{F} = & \alpha(|\eta_+|^2 + |\eta_-|^2) + \beta_1(|\eta_+|^2 + |\eta_-|^2)^2 - \beta_2(|\eta_+|^2 - |\eta_-|^2)^2 \\ & + \frac{k_0 + k_1}{2} \{|\Pi\eta_+|^2 + |\Pi\eta_-|^2\} + (k_2 + k_3) \{(\Pi_-\eta_+)^* \Pi_+\eta_- + (\Pi_+\eta_-)^* \Pi_-\eta_+\} \\ & + \frac{\mathbf{B}^2}{8\pi}, \quad (\text{S2}) \end{aligned}$$

where in the convenient notation $\hbar = c = k_B = 1$, microscopic calculations for a cylindrical Fermi surface (FS) yield $\alpha = -N(0)\ln(T_c/T)/2$, $\beta_1 = 21N(0)\zeta(3)/(8\pi T)^2$, $\beta_2 = \beta_1/3$, $k_1 = k_2 = k_3 = 7N(0)\zeta(3)v_F^2/2(8\pi T)^2$, and $k_0 = 3k_1$, with $N(0)$ being the density of states at the FS, T_c the superconducting critical temperature, $\zeta(x)$ the Riemann zeta function, and v_F the Fermi velocity [1]. Moreover, $\Pi = (\nabla - ie\mathbf{A})$ and $\Pi_{\pm} = (\Pi_x \pm i\Pi_y)/\sqrt{2}$.

The GL equations are obtained by minimization of the GL functional Eq. (S2), and are solved numerically in dimensionless form (see Ref. [2]), where all distances are scaled to the superconducting coherence length $\xi(T) = 21\zeta(3)v_F^2/(8\pi T)^2 \ln(T_c/T)$, the applied magnetic field to the bulk upper critical field $H_{c2} = \Phi_0/2\pi\xi^2$ (Φ_0 is the flux quantum), and the Cooper-pair density to the bulk superconducting gap $\Delta_0 = (8\pi T)^2 \ln(T_c/T)/56\zeta(3)$. For convenience in the dimensionless quantities $\boldsymbol{\eta}' = (\eta'_+, \eta'_-)^T$, $\boldsymbol{\Pi}'$, Π'_{\pm} , ∇' , and \mathbf{B}' , from now on we drop all the primes to write the GL equations as

$$\frac{2}{3} \begin{bmatrix} \Pi^2 & \Pi_+^2 \\ \Pi_-^2 & \Pi^2 \end{bmatrix} \boldsymbol{\eta} + [1-f(\beta)|\boldsymbol{\eta}|^2 + g(\beta)(\boldsymbol{\eta}^* \hat{\sigma}_z \boldsymbol{\eta}) \hat{\sigma}_z] \boldsymbol{\eta} = 0, \quad (\text{S3})$$

$$\kappa^2 \nabla \times \nabla \times \mathbf{A} = \mathbf{J}, \quad (\text{S4})$$

where $\hat{\sigma}_z$ is the z Pauli matrix, $f(\beta) = (1 - \beta)^{-1}$ and $g(\beta) = \beta(1 - \beta)^{-1}$ are parameter functions depending on $\beta = \beta_2/\beta_1 = 1/3$, \mathbf{J} is the superconducting current density, and $\kappa = \lambda/\xi$ is the GL parameter, with λ being the London penetration depth. We take for κ the in-plane value of bulk SRO ($\kappa = 2.6$). Eq. (S4) is solved in 3D, taking the sample thickness into account following the Fourier approach described in Ref. [3].

The boundary conditions imposed on the components of the order parameter assumes specular reflection at the edges. They are obtained from the conditions that $\boldsymbol{\eta} \cdot \hat{\mathbf{n}} = 0$, and $\mathbf{J} \cdot \hat{\mathbf{n}} = 0$, where $\hat{\mathbf{n}}$ is a unitary vector normal to the boundary, and \mathbf{J} is the superconducting current density. For the considered ring geometry of the sample, polar coordinate system is a convenient choice to solve the GL equations. Then, the supercurrent density is calculated by

$$J_\rho = \frac{2}{3} \text{Im} \left\{ [\eta_+^* \Pi_\rho \eta_+ + \eta_-^* \Pi_\rho \eta_-] + \frac{1}{\sqrt{2}} [\eta_+^* e^{i\phi} \Pi_+ \eta_- + \eta_-^* e^{-i\phi} \Pi_- \eta_+] \right\}, \quad (\text{S5})$$

$$J_\phi = \frac{2}{3} \text{Im} \left\{ [\eta_+^* \Pi_\phi \eta_+ + \eta_-^* \Pi_\phi \eta_-] + i \frac{1}{\sqrt{2}} [\eta_+^* e^{i\phi} \Pi_+ \eta_- - \eta_-^* e^{-i\phi} \Pi_- \eta_+] \right\}. \quad (\text{S6})$$

The GL equations (S3) and (S4) are solved in polar coordinates using finite differences on a uniformly spaced grid. Solutions to this equation are obtained by the iterative relaxation method, over time steps scaled to the Ginzburg-Landau time $\tau_{\text{GL}} = \xi^2/D$, where D is diffusion constant. A large variety of initial inputs are provided to the algorithm to evaluate the stability of different solutions, and compare their free energy to find the ground state of the system.

The energy density (scaled to the condensation energy $F_0 = H_c^2 V/4\pi$, V being the volume of the sample) used for the determination of the ground state is calculated after multiplication of Eq. (3) by $\boldsymbol{\eta}^*$ from the left-hand side,

$$\frac{2}{3} (\boldsymbol{\eta}^* \Pi^2 \boldsymbol{\eta} + \boldsymbol{\eta}^* [\Pi_+^2 \hat{\sigma}_+ + \Pi_-^2 \hat{\sigma}_-] \boldsymbol{\eta}) + |\boldsymbol{\eta}|^2 - f(\beta)|\boldsymbol{\eta}|^4 + g(\beta)(\boldsymbol{\eta}^* \hat{\sigma}_z \boldsymbol{\eta})^2 = 0, \quad (\text{S7})$$

where the matrices $\hat{\sigma}_{\pm} = (\hat{\sigma}_x \pm i\hat{\sigma}_y)/2$ have been introduced to simplify the notation. Straightforward calculations yield following expressions, useful to transform second-order derivatives into kinetic energy densities,

$$\boldsymbol{\eta}^* \Pi^2 \boldsymbol{\eta} = \nabla \cdot (\boldsymbol{\eta}^* \Pi \boldsymbol{\eta}) - (\Pi \boldsymbol{\eta})^* \Pi \boldsymbol{\eta} \quad (\text{S8})$$

$$\boldsymbol{\eta}^* [\Pi_+^2 \hat{\sigma}_+ + \Pi_-^2 \hat{\sigma}_-] \boldsymbol{\eta} = \partial_+ (\boldsymbol{\eta}^* \hat{\sigma}_+ \Pi_+ \boldsymbol{\eta}) + \partial_- (\boldsymbol{\eta}^* \hat{\sigma}_- \Pi_- \boldsymbol{\eta}) - \{(\Pi_- \eta_+)^* \Pi_+ \eta_- + (\Pi_+ \eta_-)^* \Pi_- \eta_+\}. \quad (\text{S9})$$

The divergence term and the derivatives involving ∂_{\pm} in Eqs. (S8) and (S9), where $\partial_{\pm} = (\partial_x \pm i\partial_y)/\sqrt{2}$, are discarded since they transform into vanishing surface terms. The substitution of the remaining terms into Eq. (S7) yields

$$\frac{2}{3} (|\Pi \eta_+|^2 + |\Pi \eta_-|^2 + \{(\Pi_- \eta_+)^* \Pi_+ \eta_- + (\Pi_+ \eta_-)^* \Pi_- \eta_+\}) = |\boldsymbol{\eta}|^2 - f(\beta) |\boldsymbol{\eta}|^4 + g(\beta) (\boldsymbol{\eta}^* \hat{\sigma}_z \boldsymbol{\eta})^2, \quad (\text{S10})$$

which one can use to substitute the kinetic energy densities in the dimensionless form of Eq. (S2), and subsequently integrate to obtain the reduced free energy expression

$$F = -\frac{1}{2} \int (|\eta_+|^4 + |\eta_-|^4) dV - \frac{1+\beta}{(1-\beta)} \int |\eta_+|^2 |\eta_-|^2 dV + \kappa^2 \int B^2 dV, \quad (\text{S11})$$

where V is the dimensionless volume of the sample.

The GL formalisms for chiral p -wave and chiral d -wave superconductors have analogous form, and the discussion here is applicable to both systems.

B. Energetics behind domain-wall formation under mesoscopic confinement

For ring-shaped samples where the internal radius is kept fixed ($r_{\text{in}} = 2\xi$) and the external radius (r_{out}) is varied, the energy dependence on r_{out} for a mono-domain state and a chiral domain-wall state (ChDW) is shown in Supplementary Figure 2. We also show the state with a circular domain-wall, that was predicted in Ref. [4] to be stable in mesoscopic samples, but exhibits much high energy in our case.

In Supplementary Figure 2 the state with one ChDW is the ground state of the system for $r_{\text{out}} < 7.7\xi$, and the mono-domain state becomes the ground state for $r_{\text{out}} > 7.7\xi$. Bearing in mind the temperature- and thickness- dependence of κ in real samples, we considered a range of values from 1 to very large, but the threshold r_{out} changed by not more than 10% (and we verified that for all the phases reported in Fig. 3d of the main manuscript). This small change in the threshold r_{out} indicates the robustness of the reported ground states of the samples to magnetic screening (at least in absence of applied magnetic field).

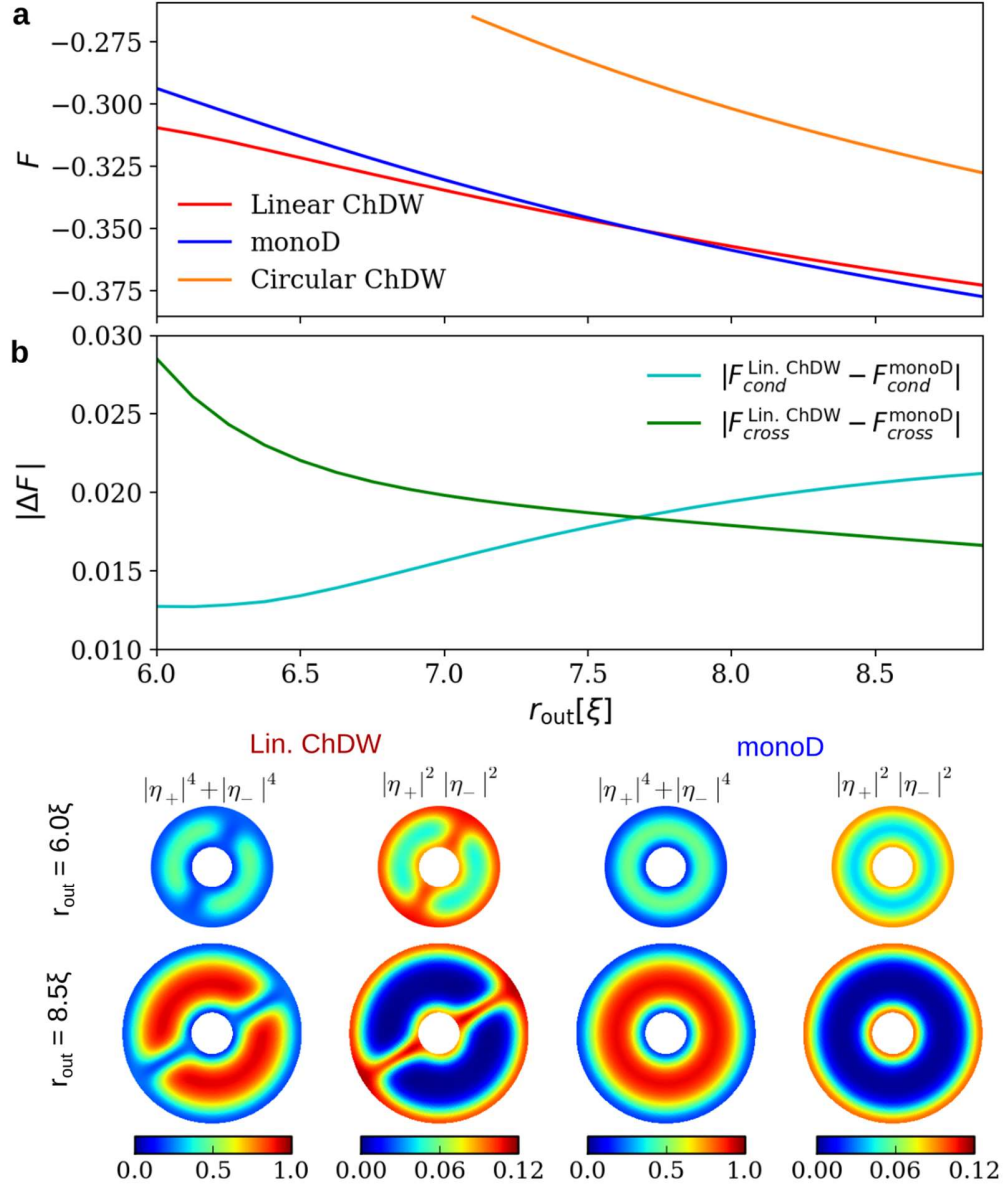
To explain the mechanism behind the domain wall formation in what follows we analyze the contributions to the free energy of the system, using simplified expression of Eq. (S11). First, we note that the third term of Eq. (S11) has negligible (two orders of magnitude lower) values compared to the other two, in absence of applied magnetic field. Our calculated fields stemming from spontaneous currents, and their energy, are in accordance with earlier analysis of Ref. [5], for p -wave slabs. Although with weak contribution to total energy, the stray magnetic field of different states in Supplementary Figure 2 can serve as a mean for their identification in scanning-probe experiments. For that reason, we show in Supplementary Figure 3 the contour plots of the calculated distribution of Cooper-pair density (relevant to STM/STS) and the magnetic induction (relevant to MFM, SOT, SHPM) of those states.

To understand the physical significance of the remaining two terms in Eq. (S11), we show in Supplementary Figure 2 the contour plots of the energy densities corresponding to those terms, *i.e.* $\mathcal{F}_{\text{cond}} = |\eta_+|^4 + |\eta_-|^4$, and $\mathcal{F}_{\text{cross}} = |\eta_+|^2|\eta_-|^2$, for two sizes of the ring, namely $r_{\text{out}} = 6\xi$ and $r_{\text{out}} = 8.5\xi$, for both the mono-domain (conventional Meissner) and the ChDW state.

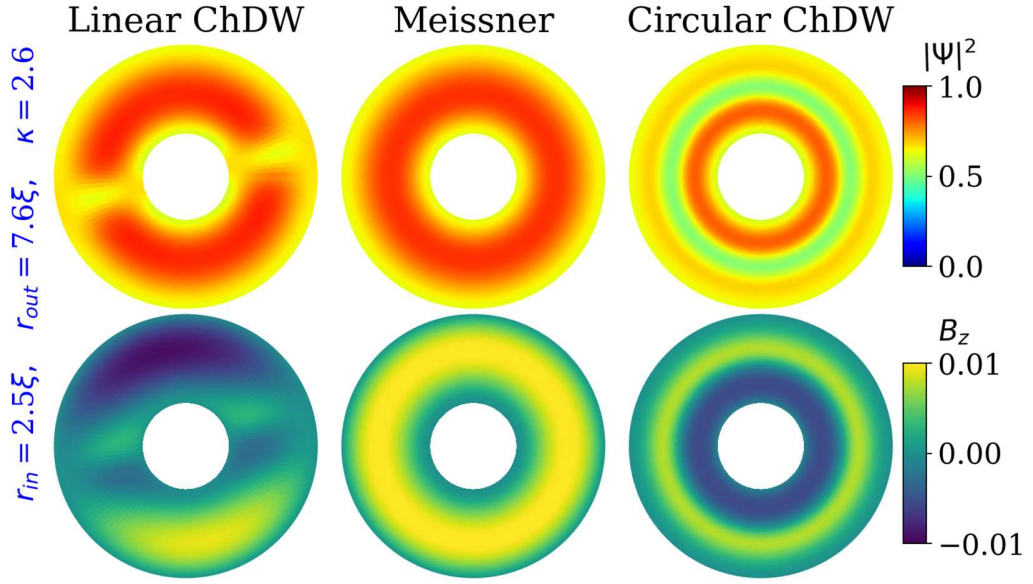
It is rather obvious that the energy density $\mathcal{F}_{\text{cond}}$ is maximal (minimal) wherever the Cooper-pair density is maximal (minimal). As a consequence, $\mathcal{F}_{\text{cond}}$ of the mono-domain state will always be lower than the one of the ChDW state, owing to the suppression of Cooper-pair density at the domain wall, since the suppression of Cooper-pair density (CPD) at the edges of the sample is nearly identical in the two states. In smaller samples, the $\Delta\mathcal{F}_{\text{cond}}$ contribution due to domain wall decreases as the suppression of CPD at the edges occupies more of the sample in both states, and the domain wall becomes shorter.

On the other hand, the energy density $\mathcal{F}_{\text{cross}}$ exhibits exactly opposite behavior to that of $\mathcal{F}_{\text{cond}}$. $\mathcal{F}_{\text{cross}}$ is maximal wherever two chiral components coexist, *i.e.* at the sample edges and along the ChDW. $\mathcal{F}_{\text{cross}}$ contribution increases as the sample is made smaller, but faster in the presence of a chiral domain wall, since then two chiral components (and associated spontaneous currents) become more spread over the sample.

To show this directly, in Supplementary Figure 2b we plot the energy differences $|\Delta F_{\text{cond}}| = |F_{\text{cond}}^{\text{ChDW}} - F_{\text{cond}}^{\text{monoD}}|$ and $|\Delta F_{\text{cross}}| = |F_{\text{cross}}^{\text{ChDW}} - F_{\text{cross}}^{\text{monoD}}|$ as a function of the sample size (outer radius). One can see that while $|\Delta F_{\text{cross}}|$ is the leading (largest) term in the energy for $r_{\text{out}} < 7.7\xi$, the condensation energy difference $|\Delta F_{\text{cond}}|$ dominates for $r_{\text{out}} > 7.7\xi$. In other words, the competition between these two energy terms directly determines the ground state of the system in absence of applied magnetic field.



Supplementary Figure 2. (a) Energy dependence of the mono-domain (Meissner) state and the state with one chiral domain wall (ChDW) for ring samples with $r_{\text{in}} = 2\xi$ and varied r_{out} . For comparison, the energy of the state with a circular domain wall is also shown, albeit significantly higher. (b) Condensation and crossing energy difference (ΔF_{cond} and ΔF_{cross} respectively) between the mono-domain (Meissner) state and the ChDW state. Panel (c) shows the spatial distribution of F_{cond} and F_{cross} , for samples with $r_{\text{out}} = 6.0\xi$ and $r_{\text{out}} = 8.5\xi$ in the Meissner state and the ChDW state.

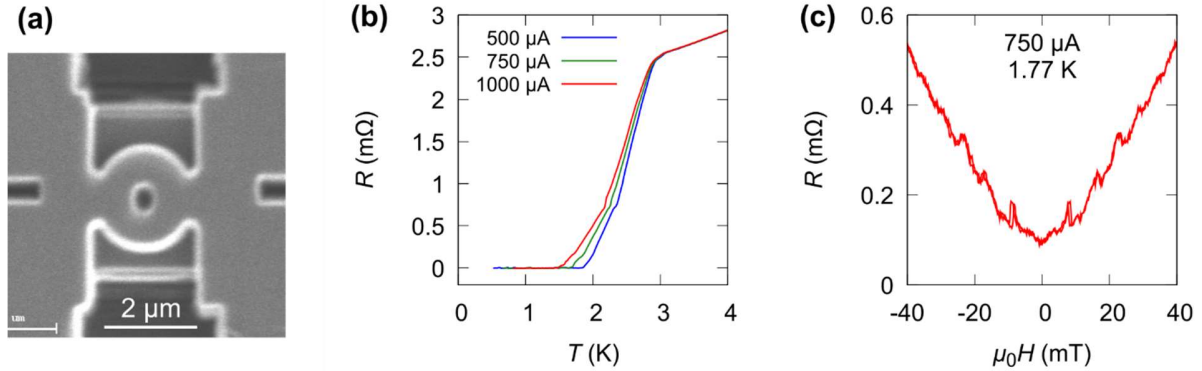


Supplementary Figure 3. Contour plots of the total Cooper-pair density and the magnetic induction for different states of Supplementary Figure 2a.

Supplementary Note 3.

ANOTHER EXAMPLE OF A RING IN THE EXTRINSIC PHASE

In this section, we show another ring (Ring D) in the extrinsic phase. Since this crystal was not covered with SiO₂ protection layer before FIB, the onset T_c is higher than the other rings as shown in Supplementary Figure 4b, namely the ring is in the extrinsic (3-K) phase. Supplementary Figure 4c shows magnetoresistance $R(H)$ just above the zero-resistance T_c . The amplitude is not as large as that of a SQUID ring (Ring A). Therefore, the magnetoresistance oscillations of Ring D are considered to be the Little-Parks oscillations. We note the peaks appear non-periodically because the arm width $w = r_{\text{out}} - r_{\text{in}}$ is much wider than the coherence length, and hence the ring is outside the London limit [6].



Supplementary Figure 4. Results of Ring D. (a) Scanning ion microscope image. (b) Resistance as a function of temperature $R(T)$. (c) Resistance as a function of magnetic field $R(H)$ at a temperature in the transition region. The amplitude of the magnetoresistance oscillations is much smaller than those of the rings without the extrinsic phase e.g. Ring A (see Fig. 5 in the main text).

Supplementary Note 4.

EVIDENCE OF DOMAIN WALL RECONFIGURATION

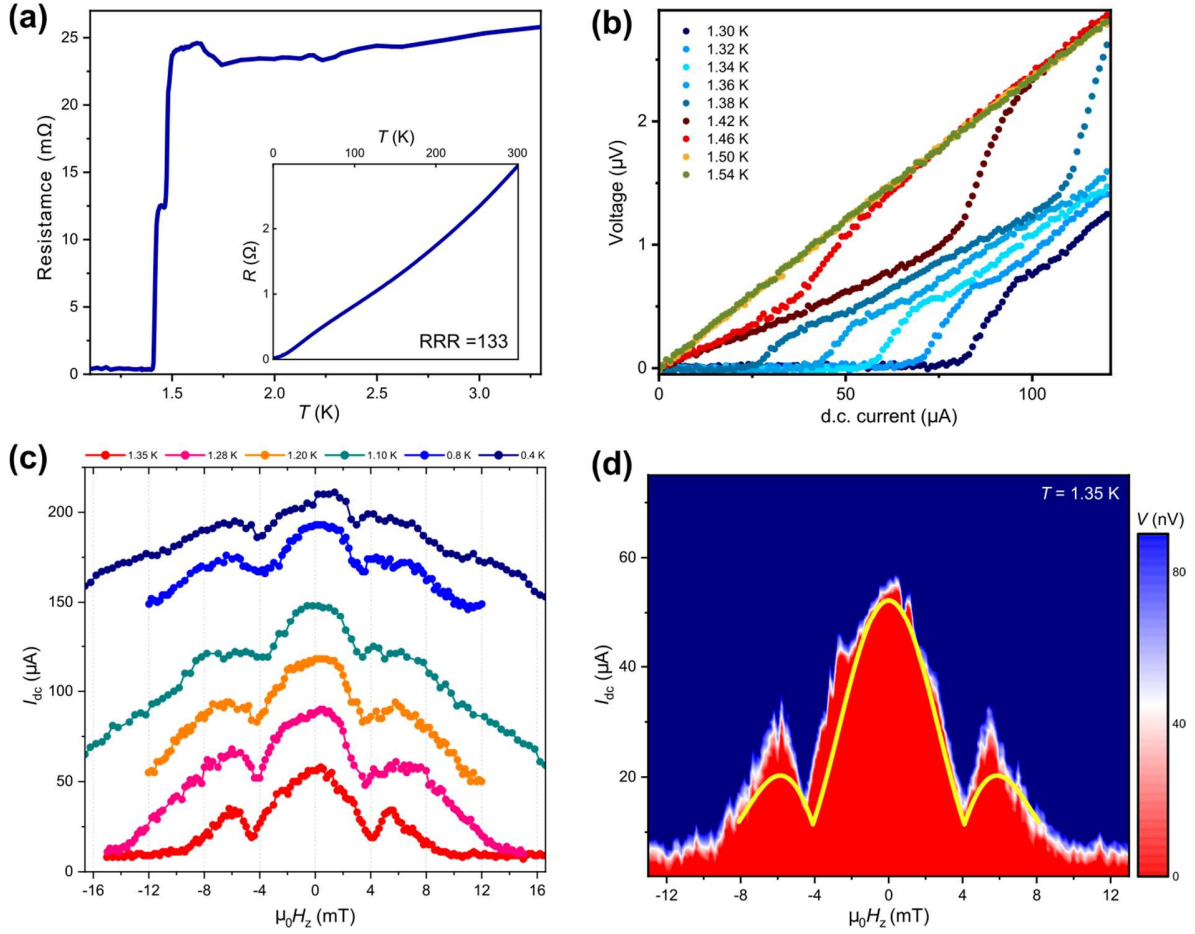
As shown in Fig. 3 of the main text, the Josephson junctions formed at the domain wall can take on a number of stable arrangements, depending on the size of r_{in} and r_{out} relative to $\xi(T)$. Most of these states result in the formation of parallel Josephson junctions in the arms of the ring, which would appear as SQUID oscillations in our transport measurements. Such is the case for Rings A and B, where any one of the simulated states for their given dimensions (1ChDW, 2ChDW and the extended ChDW depending on temperature) would yield similar SQUID oscillations, where the states cannot be distinguished from one another.

To find evidence of alternative domain configurations, we explore left side of the calculated phase diagram in Fig. 3, using a ring with considerably wider arms (Ring E). The ring dimensions ($r_{\text{in}} = 0.15 \mu\text{m}$, $r_{\text{out}} = 0.54 \mu\text{m}$) are chosen so that a ChDW would be energetically stable for an appreciable temperature range below T_c , but becomes progressively less favourable at lower temperatures as we approach the Meissner state. The results are summarised in Supplementary Figure 5.

Once again, we observe clear critical current oscillations over a wide temperature range below T_c . However, the supercurrent interference patterns differ significantly from those of Rings A and B. The distinction is perhaps most notable at $T = 1.35$ K, where the centre lobe of the $I_c(B)$ pattern is twice as wide as the side lobes, and the oscillation amplitude declines with approximately $1/B$ dependence. As shown in Supplementary Figure 5d, this $I_c(B)$ shows unambiguously the Fraunhofer pattern, which is considered as the hallmark of the Josephson effect. The observed Fraunhofer pattern serves to establish the presence of intrinsic junctions in our crystal, and hence supporting the existence of superconducting domain walls in Sr_2RuO_4 . More importantly, the contrast between the Fraunhofer diffraction and the two-channel interference patterns of Rings A and B demonstrates a clear difference in the arrangement of the junctions (i.e. domain walls) based on ring dimensions.

Since a doubly connected superconductor cannot yield a Fraunhofer diffraction by itself (not even if one of the arms contains a weak link), the junction(s) needs to be arranged in series with the loop i.e. at either side of the ring, where it joins the transport leads via the (≈ 0.45 μm wide) “necks”. While the walls of Rings A and B are considerably narrower than the leads on each side, arms of Ring E and the leads connected to it are comparable in width. It is therefore reasonable for domain walls to emerge from the constrictions on the sides of the ring rather than its centre. This also suggests that the domain walls are not pinned as strongly as those for Rings A and B. While this particular domain configuration is absent in the phase diagram of Fig. 3, we attribute this to the finite size of our simulations which do not capture the full effect of the large sections of the crystal connected to each side of the ring.

Also noteworthy is the evolution of the $I_c(B)$ pattern as we lower the temperature. Supplementary Figure 5c shows a substantial dampening of the oscillations as we approach the mono-domain (Meissner) state in Fig. 3. Note that even at $T = 400$ mK, where $\frac{r_{\text{in}}}{\xi(T)} \approx 2$ and $\frac{r_{\text{out}}}{\xi(T)} \approx 7$, the equilibrium Meissner state still has a slightly higher energy than one with a ChDW. However, the external magnetic fields applied while measuring $I_c(B)$ could tip this balance by pushing the domain wall outside our system.



Supplementary Figure 5. Josephson effect in a ring with wider arms. (a) Resistance as a function of temperature $R(T)$ for Ring E ($r_{\text{in}} = 0.15 \mu\text{m}$, $r_{\text{out}} = 0.54 \mu\text{m}$), measured with a $10 \mu\text{A}$ bias. The large residual resistivity ratio (RRR = 133) shows the high metallicity of the system. (b) Current-voltage measurements taken at different temperatures. Superconductivity emerges at 1.47 K, close to the T_c of bulk Sr_2RuO_4 . (a) and (b) both indicate the complete absence of the extrinsic 3 K-phase. (c) Critical current as a function of out-of-plane magnetic field, measured at different temperatures. A Fraunhofer pattern is observed near T_c , where the center lobe (8.5 mT) is twice as wide as the side lobes (≈ 4 mT). This is shown more clearly in (d), where the data taken at $T = 1.35$ K is fitted with a Fraunhofer diffraction pattern. As the temperature is lowered to 0.4 K, ($\frac{r_{\text{in}}}{\xi(T)} \approx 2$, $\frac{r_{\text{out}}}{\xi(T)} \approx 7$) domain wall states become energetically less favourable in our system (see Supplementary Figure 2). Consequently, the $I_c(B)$ oscillations – driven by the Josephson effect at the domain wall – begin to fade away.

Supplementary References

- [1] J.-X. Zhu, C. S. Ting, J. L. Shen, and Z. D. Wang, *Ginzburg-Landau equations for layered p-wave superconductors*, Phys. Rev. B **56**, 14093 (1997).
- [2] V. Fernandez Becerra, E. Sardella, F. M. Peeters, and M. V. Milosevic, *Vortical vs skyrmionic states in mesoscopic p-wave superconductors*, Phys. Rev. B **93**, 014518 (2016).
- [3] M. V. Milošević and R. Geurts, *The Ginzburg–Landau theory in application*, Physica C **470**, 791 (2010).
- [4] V. Vakaryuk, *Stability of topological defects in chiral superconductors: London theory*, Phys. Rev. B **84**, 214524 (2011).
- [5] A. Furusaki, M. Matsumoto, and M. Sigrist, *Spontaneous Hall effect in a chiral p-wave superconductor*, Phys. Rev. B **64**, 054514 (2001).
- [6] V. Bryundoncx, L. Van Look, M. Verschuere, and V. V. Moshchalkov, *Dimensional crossover in a mesoscopic superconducting loop of finite width*, Phys. Rev. B **60**, 10468 (1999).